applied sciences

MDPI

Article

Numerical Investigation of Heat Transfer Augmentation in Axial and Parallel Rotating Channels with Inserts

Kofi Yeboah Asante [1], Abraham Adu-Mills [1], Yashitha Thuraka [1], Obed Y. W. Abotsi [1], Richard Opoku [2] and John P. Kizito [1,*]

[1] Department of Mechanical Engineering, North Carolina Agricultural and Technical State University, Greensboro, NC 27411, USA
[2] Department of Mechanical Engineering, Kwame Nkrumah University of Science and Technology (KNUST), Kumasi AK-448-7139, Ghana
* Correspondence: jpkizito@ncat.edu

Abstract

Rotating cooling channels are an effective way to enhance convective heat transfer in high-speed, high-power-density electric machines. This study numerically investigates the flow and heat transfer in axial and parallel rotating channels across a range of axial Reynolds numbers (Re_a = 5000–25,000) and rotation numbers (N = 1–3). The numerical study is conducted using three-dimensional RANS simulations with the realizable k-ϵ model, validated against established rotating pipe correlations. Parallel rotation consistently produces higher heat transfer enhancement than axial rotation under identical operating conditions, with the Nusselt number (Nu) increasing with the eccentricity ratio (H/D). The largest enhancement is observed for the parallel configuration at H/D = 8, where Nu increases by 88% compared to the axial case at Re_a = 5000 and N = 3, resulting from amplified centrifugal forces that generate intense secondary vortices. The effect of a Kenics static mixer is also evaluated in both configurations. The insert enhances Nu by 17–38% in axial channels, where rotational effects alone are insufficient to promote strong secondary flow, but produces only marginal gains of 0–8% in parallel channels at H/D = 8, despite a significant increase in pressure drop. Thermal Performance Factor (TPF) analysis against the stationary pipe benchmark reveals that all empty pipe rotating configurations achieve TPF > 1, reaching a maximum of 1.47 for the parallel H/D = 8 configuration at Re_a = 5000 and N = 3, while all Kenics-equipped configurations produce TPF < 1 throughout the study. The scientific contribution of this study is twofold. First, the Kenics mixer provides substantial heat-transfer enhancement that is strongest in axial channels and diminishes with increasing eccentricity (0–8% at H/D = 8). Second, despite this heat-transfer enhancement, the Kenics-equipped configurations yield TPF < 1 in every case examined, meaning Nu gains do not offset the associated pressure penalty on a performance-weighted basis. By contrast, the empty rotating configurations—particularly parallel rotation at high eccentricity—achieve TPF > 1 up to 1.47 (H/D = 8, Re_a = 5000, N = 3). These results indicate that rotation alone is the preferred augmentation strategy when overall thermo-hydraulic performance is the design objective, while Kenics inserts should be reserved for applications where maximum heat-transfer enhancement is prioritized over the pressure penalty.

Keywords: axial rotation; parallel rotation; Kenics mixer; secondary flows; rotating channels

Check for updates

Received: 23 September 2026
Revised: 23 October 2026
Accepted: 27 October 2026
Published: 29 October 2026

Copyright: © 2026 by the authors. Licensee MDPI, Basel, Switzerland. This article is an open access article distributed under the terms and conditions of the Creative Commons Attribution (CC BY) license.

1. Introduction

Efficient thermal management is critical for high-power-density systems, particularly in hybrid-electric propulsion applications. Such machines generate substantial heat within the windings, rotor, and permanent magnets, and the dense packaging and high rotational speeds characteristic of modern designs mean that this heat must be removed effectively to maintain performance and reliability [1]. The achievable power density of an electrical machine is in fact strongly limited by the effectiveness of its cooling system, as rising loss densities and shrinking cooling surface areas accompany any increase in power density [2]. Inadequate rotor cooling can elevate magnet temperatures beyond their operating limits, leading to decreased torque output, reduced efficiency, and demagnetization and insulation failure [1]. Hybrid-electric aircraft offer a promising route to reduce this footprint by combining electric and conventional propulsion, which lowers emissions, improves propulsion efficiency, reduces operating and maintenance costs, and cuts airport noise. Realizing these benefits, however, depends on effectively cooling the high-speed, high-power-density electric motors at the core of such systems, where substantial heat is generated within the windings, rotor, and permanent magnets [3].

The rotors in these machines are typically cooled by passing fluid through internal channels within the shaft. The introduction of rotation to an internal flow essentially changes basic physics. As the channel walls impart angular momentum to the adjacent fluid, a tangential velocity component develops that has no counterpart in non-rotating systems. A configuration in which the pipe rotates about its own longitudinal axis is referred to as an axial rotational configuration (Figure 1). A foundational contribution was made by Pedley et al. [4], who demonstrated that the Hagen–Poiseuille velocity profile in an axial rotating pipe becomes susceptible to small perturbations once the pipe is set to rotate about its central axis. Borisenko et al. [5] reported that pipe rotation dampens turbulence intensity, particularly near the pipe centerline. The hydraulic resistance implications of axial rotation were first investigated by White [6], who demonstrated that axial rotation decreases frictional losses by up to 40% at high axial Reynolds numbers. Seghir-Ouali et al. [7] experimentally investigated heat transfer in an axial rotating cylinder and observed a continuous increase in the Nusselt number (Nu) with increasing rotation rate.

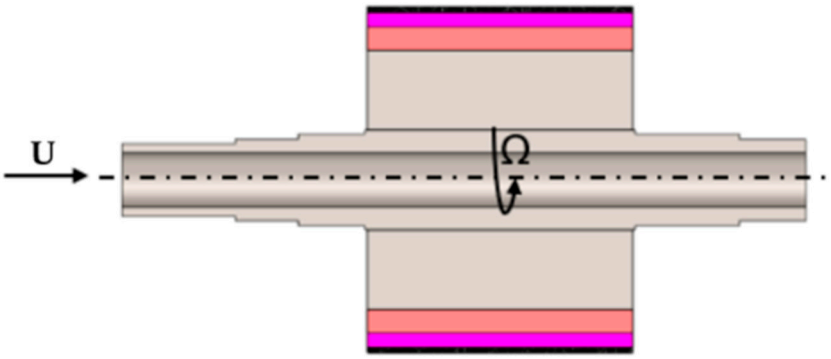


Figure 1. Cross-section of a rotor with an axial rotating cooling channel, representative of high-power-density electric machines such as the 1 MW rotor of [8], with losses of approximately 4600 W in the sleeve, 1000 W in the magnets, and 180 W in the core at 20,000 rpm. Color key: pink, rotor magnets; light gray, rotor core; dark gray, carbon fiber sleeve. U denotes the coolant bulk (inlet) velocity, and Ω denotes the angular velocity of rotation.

In parallel rotation, however, the axis of the cooling channel is offset from the axis of the rotating shaft, with the two axes remaining parallel in geometry (Figure 2). Humphrey et al. [9] reported significant Nu enhancement in a pipe rotating in parallel configuration under both uniform wall temperature and uniform heat flux conditions, with Coriolis forces

and inlet swirl identified as contributing mechanisms. Morris et al. [10] reported lower heat transfer enhancement in square ducts than in circular pipes with an equivalent hydraulic diameter. Fasquelle et al. [11] investigated the influence of cross-sectional geometry under parallel rotation and found a 45% increase in Nu for an elliptical duct compared to a circular tube.

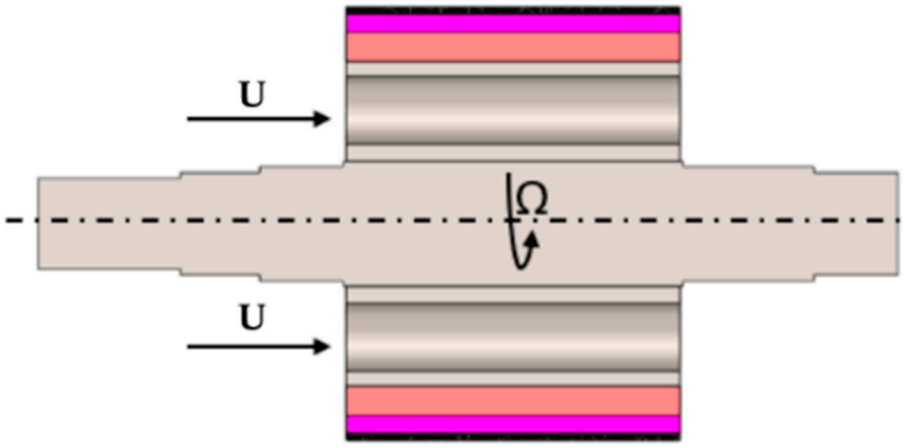


Figure 2. Cross-section of a rotor with parallel rotating cooling channels, representative of high-power-density electric machines such as the 1 MW rotor of [8], with losses of approximately 4600 W in the sleeve, 1000 W in the magnets, and 180 W in the core at 20,000 rpm. Color key: pink, rotor magnets; light gray, rotor core; dark gray, carbon fiber sleeve. U denotes the coolant bulk (inlet) velocity, and Ω denotes the angular velocity of rotation.

In some rotor configurations, both axial and parallel cooling channels exist [12]. While the effects of rotation in parallel cooling channels have been studied, the literature on the impact of the eccentricity ratio (H/D) on flow behavior and heat transfer remains limited. The eccentricity ratio (H/D) is the radial offset H of the pipe from the rotation axis, normalized by the pipe diameter D.

Inserts are widely employed to induce swirl flow and intensify turbulence, thereby improving fluid mixing and enhancing the thermal performance of cooling channels. Garg et al. [13] conducted a comprehensive review of the effects of stationary twisted tape inserts on heat transfer augmentation in stationary channels and found that convective heat transfer is enhanced through swirl and secondary flows, with the Nusselt number rising as the twist ratio decreases at the cost of a higher friction factor. Several studies have investigated the effect of rotating twisted tape inserts on the thermal performance of stationary channels. Kumar et al. [14] reported a 102.54% increase in Nu at a 60° vane angle using rotating twisted tapes. The effect of pitch distance in rotating twisted tape inserts was examined by Arasteh et al. [15], who obtained the highest heat transfer enhancement of about 63.8% at Re_a = 1000. Similarly, Song et al. [16] studied rotating twisted tapes in an elliptical duct under laminar flow (Re_a = 50–1000), reporting a 24–179% enhancement in Nu and a 50–250% increase in the friction factor.

Beyond twisted tapes, other insert-based approaches have demonstrated considerable enhancement potential. Nakhchi et al. [17] experimentally evaluated rotating elliptical inserts in double-pipe heat exchangers and found that perforated rotating inserts outperformed their non-rotating counterparts, demonstrating a 30.7% improvement in thermal transport. Dabestani et al. [18] investigated the thermal performance of heat exchangers employing spirally coiled tubes. Their results showed that rotation increased the Nu of the heated flow by more than 145%, with the enhancement being more pronounced in tubes of a smaller diameter than in larger ones. Fang et al. [19] studied a double-helical-finned coaxial heat exchanger in four fin configurations, showing that counter-rotating helical

fins achieved about a 35% increase in Nu. Taylor–Couette instabilities in concentric and eccentric annular systems have similarly demonstrated substantial Nu increases, with some configurations recording enhancements of up to 300% [20–22].

The rotational effects in rectangular and non-circular cooling channels, particularly for gas turbine blade cooling with ribs, dimples, pin fins, and vane structures, have been extensively studied, with findings showing simultaneous improvements in thermal performance compared to stationary conditions [23–29]. Channel orientation under rotation further influences thermal performance. Chia et al. [30] experimentally investigated the heat transfer distribution on the internal blade tip wall of a rotating cooling channel and reported a heat transfer enhancement of up to 68% due to rotational effects. In a related study, Zhang et al. [31] observed a spanwise increase in Nu of up to 58.5% in selected regions of a three-pass serpentine passage.

Most directly relevant to the present study are investigations into axial rotating smooth pipes. Abotsi et al. [32,33] investigated turbulent heat transfer in axial rotating pipes, both with and without inserts, reporting Nusselt number enhancement of up to 92%. Their studies also showed that, for comparable geometries, axial Reynolds numbers, and rotation rates, Kenics mixers produced greater heat transfer enhancement than twisted tape. Beyond pipe flow, significant thermal enhancement due to rotational effects has also been reported in cooling channels with ribs [34,35] and microchannels [36,37]. Although axial and parallel rotating channels have each been studied independently, a systematic comparison between them across varying eccentricities, with and without inserts, has not yet been reported. The present work aims to address this gap.

The present work contributes to the literature by (i) evaluating how axial and parallel rotating configurations affect heat transfer and pressure drop across a range of rotation rates (N) and axial Reynolds numbers (Re_a); (ii) quantifying the influence of the eccentricity ratio (H/D) on secondary flow behavior, Nusselt number, and friction factor in parallel rotating channels; and (iii) assessing the effect of Kenics static mixer inserts on heat transfer enhancement in both configurations.

2. Materials and Methods

2.1. Geometry and Configurations

A three-dimensional cylindrical duct, as shown in Figure 3, was used to investigate the effect of rotational motion on thermal and fluid characteristics. Two configurations were examined: (i) axial rotation, in which the pipe spins about its own longitudinal axis, imparting a tangential velocity to the fluid inside it, and (ii) parallel rotation, in which the pipe rotates about an axis offset from but parallel to its centerline, generating a different secondary flow structure and thermal behavior. It is important to highlight that, for parallel rotation, the fluid flowing through the pipe is offset by eccentricity (H/D) from the axis of rotation. The combined influence of rotational motion and passive flow mixing was subsequently examined using a Kenics static mixer.

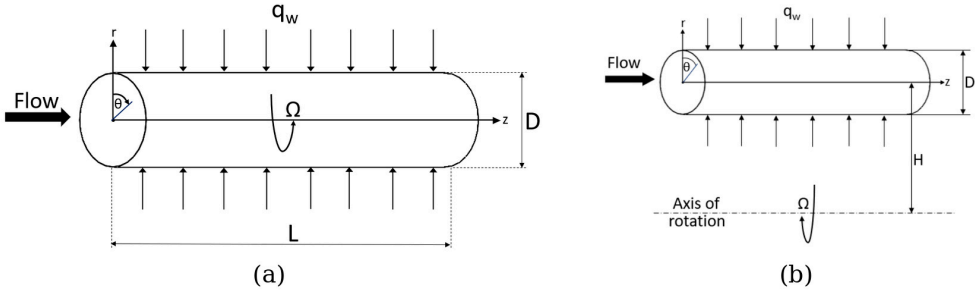


Figure 3. Schematic of the model: (**a**) axial rotation; (**b**) parallel rotation.

The pipe geometry parameters used in the present study are summarized in Table 1. Water was used as the working incompressible Newtonian fluid. The thermophysical properties of the fluid were held constant throughout the simulations, apart from density, which was treated as temperature-dependent via the Boussinesq approximation.

Table 1. Geometric parameters of the pipe.

Parameter	Symbol	Value
Diameter	D (mm)	20
Pipe Length	L (mm)	800
Aspect Ratio	L/D	40
Eccentricity Ratio	H/D	2, 4, 8

2.2. Physical Model

The flow is assumed to be steady, turbulent, and three-dimensional. The pipe wall is subjected to a uniform heat flux q_w, and the fluid enters the inlet with a bulk velocity U and a uniform temperature T_{in}. Two rotating configurations are examined, as shown in Figure 3. In configuration (a) the pipe rotates about its own axis (axial rotation). In configuration (b) the pipe axis is parallel to the axis of rotation and is offset from it by a distance H (parallel-axis rotation). In both cases the angular velocity Ω is constant and parallel to the pipe axis. Gravity acts on the fluid in both configurations, and its direction relative to the rotation axis is specified below.

The governing equations are written in a cylindrical coordinate system (r,θ,z) fixed to the pipe and rotating with it, with z along the pipe axis and θ measured from the r-axis shown in Figure 1. The unit vectors are $\mathbf{e}_r$, $\mathbf{e}_\theta$ and $\mathbf{e}_z$. In this frame the pipe wall is stationary, and the velocity $\mathbf{v}$ is the velocity relative to the rotating frame. The angular velocity vector and the position vector $\mathbf{R}$ measured from the axis of rotation are

$$\boldsymbol{\Omega} = \Omega \mathbf{e_z} \tag{1}$$

$$\mathbf{R} = \mathrm{H}\mathbf{e_h} + \mathrm{r}\mathbf{e_r}, \quad \mathbf{e}_\mathrm{h} = (\cos\theta)\mathbf{e_r} - (\sin\boldsymbol{\theta})\,\mathrm{e}_\theta \tag{2}$$

where $\mathbf{e}_h$ is the unit vector pointing from the axis of rotation to the pipe axis. Configuration (a) is recovered by setting $H = 0$. The centrifugal acceleration is then

$$-\boldsymbol{\Omega} \times \boldsymbol{\Omega} \times \mathbf{R} = \Omega^2 \mathbf{R} = \Omega^2[(\mathrm{r} + \mathrm{H}\cos\theta)\,\mathbf{e}_\mathrm{r} - \mathrm{H}\sin\theta\,\mathbf{e}_\theta] \tag{3}$$

and the Coriolis acceleration is

$$2\,\boldsymbol{\Omega} \times \mathbf{v} = 2\Omega(-\mathrm{v}_\theta\,\mathbf{e}_\mathrm{r} + \mathrm{v}_\mathrm{r}\,\mathbf{e}_\theta) \tag{4}$$

Because $\boldsymbol{\Omega}$ is parallel to z, the Coriolis force acts only on the cross-stream velocity components and does not act on the axial flow directly.

The gravity vector $\mathbf{g}$ expressed in the rotating frame depends on the orientation of the pipe. Two orientations are considered. For a vertical pipe, the rotation axis is parallel to gravity, and $\mathbf{g}$ is fixed in the rotating frame,

$$\mathbf{g} = -\mathrm{s}\,\mathrm{g}\,\mathbf{e}_\mathrm{z}, \qquad \mathrm{s} = +1|(\text{upward flow}), \quad \mathrm{s} = -1|(\text{downward flow}) \tag{5}$$

For a horizontal pipe, as drawn in Figure 1, gravity is perpendicular to the rotation axis. Gravity then appears to rotate in the relative frame with angular velocity $-\Omega$,

$$\mathbf{g} = -\mathrm{g}[\cos(\theta + \Omega\mathrm{t})\,\mathbf{e}_\mathrm{r} - \sin(\theta + \Omega\mathrm{t})\,\mathbf{e}_\theta] \tag{6}$$

The total body-force acceleration acting on the fluid, which combines gravity and the centrifugal acceleration for steady-state (t = 0), is

$$\mathbf{g}_{\text{eff}} = \mathbf{g} - \boldsymbol{\Omega} \times \boldsymbol{\Omega} \times \mathbf{R} = \mathbf{g} + \Omega^2 \mathbf{R} \tag{7}$$

The numerical simulations were performed in ANSYS Fluent 2024 R2 using the Single Rotating Reference Frame (SRF) approach. Frame motion is enabled on the fluid cell zone and the Relative Velocity Formulation is selected. The Coriolis and offset-dependent centrifugal acceleration terms [Equations (3) and (4)] are retained in the momentum balance independently of the Boussinesq coupling, consistent with the formulation documented [38]. The Boussinesq approximation is enabled with reference density ρ_0 at the inlet temperature T_0 and the gravity vector is specified in the global coordinate system.

The steady-state assumption was verified at the lowest investigated rotation rate (N = 1) in two quantitative checks. First, the buoyancy-to-inertia force-scale ratio evaluated from the Fluent temperature field at N = 1, Re_a = 5000, H/D = 2 is small. Using the maximum temperature rise $\Delta T = T_{max} - T_{in} \approx 79$ K obtained from the Fluent solution,

$$\frac{g\beta\Delta T D_h}{U^2} \approx 4.9 \times 10^{-2},$$

so, the buoyancy contribution is more than an order of magnitude smaller than the characteristic inertial scale $\frac{U^2}{D_h}$. We note that this is a direct dimensional ratio evaluated using the simulated temperature difference, distinct from the parameter $\frac{Gr_g}{Re_a^2}$ in Equation (23), which uses the diffusive reference scale $\Delta T_{ref} = \frac{q_w D_h}{\lambda}$. Second, a transient simulation of the empty parallel rotating channel at the same operating condition was performed with identical geometry, mesh, boundary conditions, turbulence model, and velocity formulations the steady-state calculation. The transient calculation used a second-order implicit time integration with Δt = 0.005 s (approximately 100 steps per rotation period) and a maximum of 30 iterations per time step; the simulation was advanced for 3000 steps (total simulated duration 15 s, approximately 30 rotation periods at N = 1), and integral quantities were time-averaged over the final portion of the record once statistical stationarity was reached. At this operating condition, Ω = 12.56 rad/s and the fluid transit time through the 800 mm heated section is 3.185 s, corresponding to 6.37 rotation periods per transit. The steady-state calculation yielded Nu = 50.05 and f = 0.0602; the time-averaged transient calculation yielded Nu = 50.02 and f = 0.0604, giving relative differences of 0.060% in Nu and 0.331% in f. The two checks together provide quantitative support for the steady-state approximation at the tested operating condition.

The following assumptions are made:

1. The fluid is Newtonian and incompressible. Its properties (μ, λ, c_p) are constant. The density varies linearly with temperature only in the body-force terms (Boussinesq approximation), $\rho = \rho_0[1 - \beta\,(T - T_0)]$ where ρ_0 is the reference density at the reference temperature T_0, and β is the thermal expansion coefficient.
2. The angular velocity is constant, and the pipe wall rotates with the frame, so the no-slip condition applies in the relative frame.
3. Viscous dissipation is neglected.
4. Turbulence is modelled with the Reynolds-averaged Navier–Stokes (RANS) equations, the Boussinesq eddy-viscosity hypothesis and the realizable k-ε model. The turbulent Prandtl number Pr_t is constant.

2.3. Governing Equations

The mean equations for the relative velocity v, the modified pressure p' and the temperature T are as follows (the formulation corresponds to the relative velocity formulation

for rotating reference frames in the ANSYS Fluent Theory Guide [38]. Overbars denoting Reynolds' averaging are omitted.

Continuity

$$\nabla \cdot \mathbf{v} = 0 \tag{8}$$

Momentum

$$\rho_0\left[\frac{\partial v}{\partial t} + \nabla \cdot (v\, v)\right] + 2\rho_0 \boldsymbol{\Omega} \times v = -\nabla p' + \nabla \cdot \left[(\mu + \mu_t)\left(\nabla v + \nabla v^T\right)\right] - \rho_0\, \beta\, (T - T_0)\, g_{eff} \tag{9}$$

The modified pressure absorbs the constant-density gravitational and centrifugal forces and the isotropic part of the Reynolds stress,

$$p' = p + \frac{2}{3}\rho_0 k - \rho_0\, \boldsymbol{g}\cdot\boldsymbol{x} - \frac{1}{2}\rho_0 \beta (T - T_0) g_{eff} \tag{10}$$

where $\boldsymbol{x}$ is the position vector in the rotating frame. The terms on the left-hand side of Equation (9) are the inertia and the Coriolis force. The last term on the right-hand side is the buoyancy force. It contains the gravitational buoyancy force $-\rho_0\, \beta\, (T - T_0)\boldsymbol{g}$ and the centrifugal buoyancy force $-\rho_0\, \beta\, (T - T_0)\, \Omega^2 \boldsymbol{R}$. The centrifugal buoyancy force is directed toward the axis of rotation where the fluid is hotter than T_0, so hot, light fluid near the heated wall is driven inward. With **R** from Equation (2), its components are $-\rho_0\, \beta\, (T - T_0)\Omega^2 (r + H cos\, \theta)$ in the r-direction and $+\rho_0 \beta (T - T_0)\Omega^2 H sin\, \theta$ in the θ-direction.

Energy

$$\rho_0 c_p \left[\frac{\partial T}{\partial t} + \nabla\cdot(vT)\right] = \nabla\cdot\left[\left(\lambda + \frac{c_p \mu_t}{Pr_t}\right)\nabla T\right] \tag{11}$$

The turbulent viscosity μ_t is obtained from the turbulence model in Section 2.4, and $Pr_t = 0.85$. The symbol λ denotes the thermal conductivity.

2.4. Turbulence Model: Realizable k-ε

The time-averaged equations are closed using the Reynolds-averaged Navier–Stokes (RANS) approach, with the Reynolds stresses modelled through the Boussinesq eddy-viscosity hypothesis. Turbulence is represented by the realizable k-ε model, as implemented in ANSYS Fluent [8]. This model has been validated against experimental data for several comparable rotating-flow configurations: an axially rotating pipe fitted with a Kenics mixer by Abotsi et al. [32,33], on which the present geometry is based; the cooling of rotating electrical machines [11]; rotor–stator cavities [39]; and rotating cylinders with attached disks [40]. In these studies, the predicted Nusselt numbers agreed with the measurements over a wide range of rotational Reynolds numbers.

Because the Coriolis force does not appear explicitly in the transport equations for k and ε, the effect of frame rotation must be incorporated through the model coefficients. In the realizable formulation, the eddy-viscosity coefficient C_μ is not constant but is a function of both the mean strain rate and the mean rotation rate, the latter including the rotation of the reference frame. The model also satisfies realizability constraints on the normal Reynolds stresses, ensuring that they remain physically admissible (non-negative).

Buoyancy effects are included through the Boussinesq approximation. Viscous dissipation is neglected, since the flow velocities are low and its contribution is negligible relative to that of the wall heat flux.

The transport equations for the turbulent kinetic energy k and its dissipation rate ε are

$$\nabla \cdot \left(\rho_0 \mathrm{k}\, \mathbf{v}\right) = \nabla \cdot \left[\left(\mu + \frac{\mu_t}{\sigma_k}\right)\nabla \mathrm{k}\right] + \mathrm{G_k} + \mathrm{G_b} - \rho_0 \varepsilon \tag{12}$$

$$\frac{\partial\left(\rho_0 \varepsilon\right)}{\partial \mathrm{t}} + \nabla \cdot \left(\rho_0 \varepsilon\, \mathbf{v}\right) = \nabla \cdot \left[\left(\mu + \frac{\mu_t}{\sigma_\varepsilon}\right)\nabla \varepsilon\right] + \rho_0 \mathrm{C_1 S}\varepsilon - \rho_0 \mathrm{C_2}\frac{\varepsilon^2}{\mathrm{k} + \sqrt{\nu\varepsilon}} + \mathrm{C_{1\varepsilon}}\frac{\varepsilon}{\mathrm{k}}\mathrm{C_{3\varepsilon}}\mathrm{G_b} \tag{13}$$

with

$$C_1 = \max\left[0.43, \left|\frac{\eta}{\eta+5}\right|\right], \qquad \eta = \frac{S\,k}{\varepsilon} \tag{14}$$

The eddy viscosity is

$$\mu_t = \rho_0 C_\mu \frac{k^2}{\varepsilon} \tag{15}$$

The production of turbulence by the mean shear is

$$G_k = \mu_t S^2, \qquad S = \sqrt{2S_{ij}S_{ij}}, \qquad S_{ij} = \frac{1}{2}\left(\frac{\partial v_i}{\partial x_j} + \frac{\partial v_j}{\partial x_i}\right) \tag{16}$$

Unlike in the standard k-ε model, the coefficient C_μ is not constant. It depends on the strain and rotation rates, and it is the term through which frame rotation enters the model,

$$C_\mu = \frac{1}{A_0 + A_s\, U^*\, k/\varepsilon}, \qquad U^* = \sqrt{S_{ij}S_{ij} + \tilde{\Omega}_{ij}\tilde{\Omega}_{ij}} \tag{17}$$

$$\tilde{\Omega}_{ij} = \Omega_{ij} - 2\varepsilon_{ijk}\omega_k, \qquad \Omega_{ij} = \overline{\Omega}_{ij} - \varepsilon_{ijk}\omega_k \tag{18}$$

$$A_s = \sqrt{6}\cos\phi, \quad \phi = \frac{1}{3}\cos^{-1}\left(\sqrt{6}\,W\right), \quad W = \frac{S_{ij}S_{jk}S_{ki}}{\tilde{S}^3}, \quad \tilde{S} = \sqrt{S_{ij}S_{ij}} \tag{19}$$

where $\overline{\Omega}_{ij}$ is the mean rate-of-rotation tensor viewed in the rotating frame, ω_k is the angular velocity of the frame ($\omega_z = \Omega$), and ϵ_{ijk} is the permutation symbol.

The gravitational buoyancy-production term G_b in the k transport equation is evaluated using the total body-force acceleration $\mathbf{g_{eff}}$ from Equation (7), so that both the gravitational and centrifugal contributions to buoyancy are retained in the turbulence production. In ANSYS Fluent, this is implemented via the standard buoyancy-production formulation [8], with the gravity vector in the native expression replaced by $\mathbf{g_{eff}}$ through the Boussinesq body-force term.

$$G_b = \beta \frac{\mu_t}{Pr_t}\, \mathbf{g_{eff}} \cdot \nabla T \tag{20}$$

The effect of buoyancy on the dissipation rate is controlled by

$$C_{3\varepsilon} = \tanh\left|\frac{v_\parallel}{v_\perp}\right| \tag{21}$$

where $v_\parallel$ and $v_\perp$ are the velocity components parallel and perpendicular to $\mathbf{g}_{eff}$. The model constants are given in Table 2.

Table 2. Constants of the realizable *k*-*ε* model.

$C_{1\varepsilon}$	C_2	A_0	σ_k	σ_ε	Pr_t
1.44	1.9	4.04	1.0	1.2	0.85

2.5. Dimensionless Parameters

The flow and heat transfer are characterized by the following dimensionless parameters, with $\Delta T_{ref} = \frac{q_w D}{\lambda}$ and $R_{ref} = H + \frac{D}{2}$,

$$Re_a = \frac{UD}{\nu}, \quad Re_\Omega = \frac{\Omega D^2}{\nu}, \quad N = \frac{\Omega D}{V_m}, \; Pr = \frac{\mu\, c_p}{\lambda} \tag{22}$$

where Re_a, Re_Ω, N, and Pr are axial Reynolds number, rotational Reynolds number, Rotation rate and Prandtl number respectively

$$Gr_g = \frac{\beta\,\Delta T_{ref}\, g\, D^3}{\nu^2}, \; Gr_\Omega = \frac{\beta\,\Delta T_{ref}\,\Omega^2 R_{ref}\, D^3}{\nu^2} \tag{23}$$

where Gr_g and Gr_Ω are the corresponding Gravitational Grashof number and Rotational Grashof number.

The bulk temperature at axial position z is defined as the mass-flow-weighted average of the local fluid temperature over the channel cross-section

$$T_b(z) = \frac{\int_{A_c} \rho c_p v_z \, T \, dA}{\int_{A_c} \rho c_p v_z \, dA} \tag{24}$$

where A_c is the cross-sectional area of the pipe, v_z is the axial velocity, T the local fluid temperature, ρ the density and C_p the specific heat capacity.

The local convective heat transfer coefficient is defined from the imposed wall heat flux, q_w, as:

$$h_{local} = \frac{q_w}{T_w - T_b} \tag{25}$$

where T_w is the local wall temperature and T_b is the bulk temperature. The average heat transfer coefficient is obtained as the area-weighted mean of h_{local} over the heated wall.

$$h_{avg} = \frac{1}{A_s} \int_{A_s} h_{local} \, dA \tag{26}$$

where A_s is the heated wall surface area. The average Nusselt number reported in Figures 9–15 is calculated as

$$Nu = \frac{h_{avg} D}{\lambda} \tag{27}$$

The friction factor is defined as

$$f = \left(\frac{1}{L/D} \right) \left(\frac{2\Delta P}{\rho U^2} \right) \tag{28}$$

Here, ΔP is the pressure drop across the pipe, L is the pipe length, D is the pipe diameter, ρ is the fluid density, and U is the mean flow velocity.

2.6. Numerical Method

The realizable k-ε model was selected due to its improved performance in capturing rotational and recirculating flows. The enhanced wall function was used for the near-wall treatment. An inflation layer with a first-cell height of 0.01 mm and 15 layers was applied at the fluid wall. The second-order upwind scheme discretized the convective terms, and the pressure and momentum equations were solved simultaneously throughout the computational domain. A constant fluid inlet temperature of 300 K was imposed at the inlet for a range of axial Reynolds numbers (Re_a = 5000–25,000), while a constant heat flux of 100,000 W/m^2 was applied at the pipe wall. The single stationary rotating frame technique was used to model the rotating domain, with gravitational and buoyancy effects added to the simulations. Rotation rates (N) of 1, 2, and 3 were investigated across the various axial Reynolds number ranges. Throughout all simulations, the first near-wall grid point was maintained at a y+ value < 1 to fully resolve the viscous sublayer and accurately capture the near-wall velocity and thermal gradients.

A grid independence study was conducted to ensure numerical results independent of the mesh size. Four different tetrahedral grid elements, namely, 80,616, 126,294, 234,273, and 391,108, were examined for an empty pipe at N = 1, H/D = 8, and Re_a = 5000. The percentage difference in the Nusselt number and friction factor between 234,273 and 391,108 was less than 1%, as shown in Table 3. The grid size of 234,273 elements was selected for the study due to computational cost.

Table 3. Grid independence studies for an empty pipe (H/D = 8, N = 3, and Re_a = 5000).

Mesh Count	Nu	%Change in Nu	f	% Change in f
80,616	78.18	-	0.0668	-
126,294	70.72	10.55	0.0782	14.60
234,273	65.22	8.44	0.0826	5.33
391,108	64.59	0.97	0.0834	0.96

2.7. Model Validation

To confirm the reliability of the numerical model, its predictions were validated against established empirical correlations for both axial and parallel rotating pipe flows. Validation of both configurations was essential, as the present study investigated thermal performance under axial and parallel rotation over a wide range of operating conditions.

For the axial configuration, the numerical results were compared with the empirical correlation of Seghir-Ouali et al. [7]:

$$Nu = 0.01963 Re_a^{0.9285} + 8.5101 \times 10^{-6} Re_r^{1.4513} \quad (29)$$

This is valid for $0 < Re_a < 3 \times 10^4$; $1.6 \times 10^3 < Re_r < 2.77 \times 10^5$.

For the parallel configuration, the numerical results were compared with the correlation proposed by Baudoin et al. [41]:

$$\frac{Nu}{Nu_s} = 1 + 0.46 \left(N \frac{H}{D} \right)^{1.24} \quad (30)$$

This is valid for $3000 \leq Re_a \leq 25{,}000$; $0 < \Omega < 1500$ rpm and $\frac{H}{D} = 3$.

Figure 4 shows that the numerical predictions for the axial configuration agree with the Seghir-Ouali correlation to within 5%. Similarly, Figure 5 shows that the predictions for the parallel configuration agree with the Baudoin correlation to within 8%. In both cases, the predicted Nusselt numbers follow the trends of the correlation curves closely across the entire range of rotation rates considered, confirming that the numerical model reliably captures the heat transfer behavior of both axial and parallel rotating pipe flows and lending confidence to the parametric results presented in the following sections.

To establish a baseline for comparison, additional simulations were performed on a stationary smooth pipe (N = 0) for Re_a = 5000–25,000. The stationary simulations used the same geometry parameters (as shown in Table 1), mesh (as shown in Table 3), thermophysical properties, and turbulence model as the rotation cases but with rotation disabled. The resulting stationary Nusselt number Nu_0 and friction factor f_0 values, reported in Table 4, served as the reference benchmark against which the TPF was calculated.

Table 4. Stationary empty pipe reference values.

Re_a	Nu_0	f_0
5000	43.1	0.0506
10,000	67.51	0.0391
15,000	85.65	0.0344
20,000	100	0.0316
25,000	111.1	0.0292

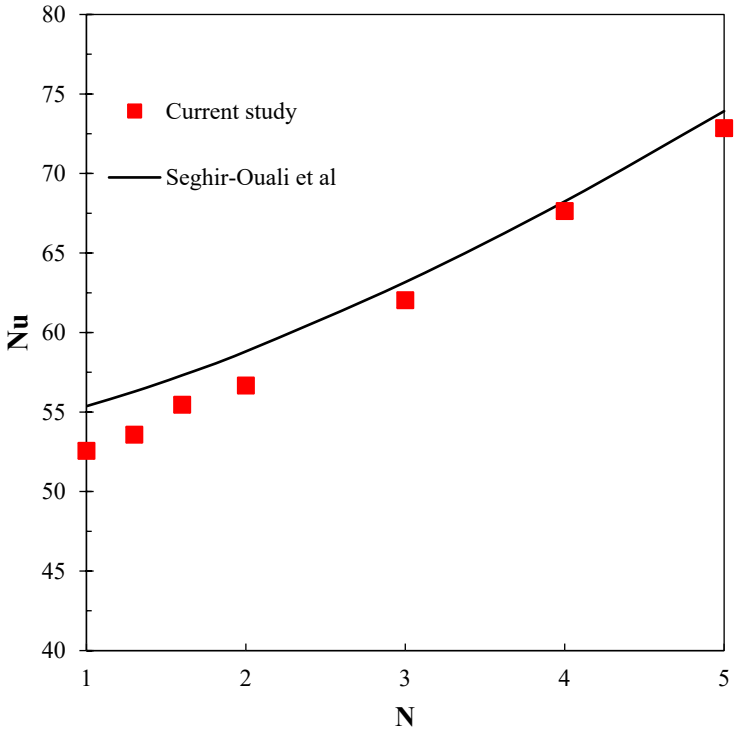


Figure 4. Validation of the model using the Seghir-Ouali correlation for axial rotation.

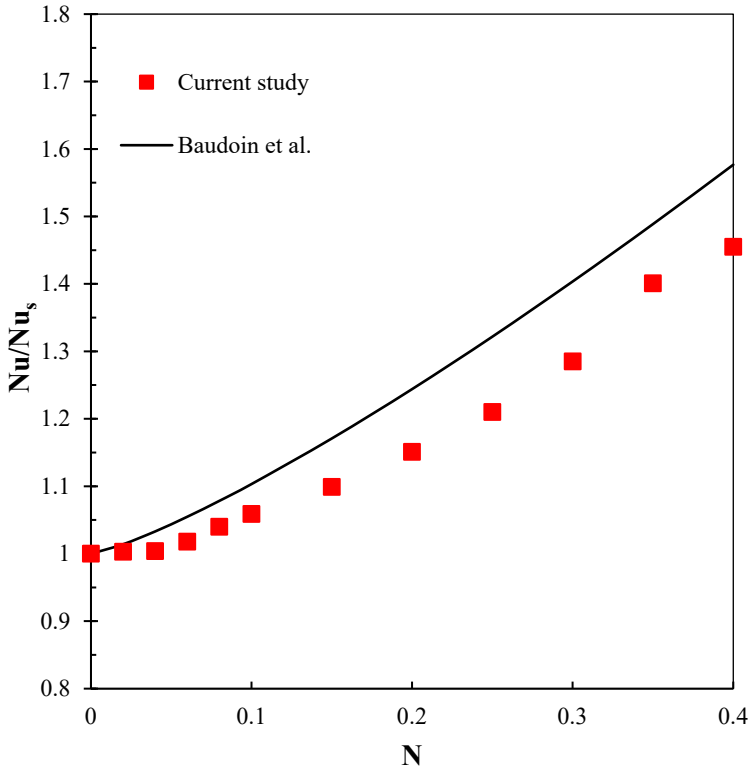


Figure 5. Validation of the model using the Baudoin correlation for parallel rotation.

2.8. Kenics Mixer Insert

A Kenics static mixer was incorporated into both the axial and parallel rotating configurations, as shown in Figure 6. The mixer geometry was constructed as a three-dimensional solid and Boolean-subtracted from the fluid domain, so that the flow is fully resolved around the surfaces. No-slip, adiabatic boundary conditions are applied on all surfaces,

while the uniform wall heat flux boundary of Section 2.3 is applied only on the outer channel wall. The objective was to investigate the combined effects of rotational motion and passive mixing induced by the insert on flow behavior, heat transport, and pressure drop. The geometry of the Kenics mixer employed in the present study was adopted from Abotsi et al. [32,33], and the geometry parameters are shown in Table 5. To ensure a consistent basis for comparison, the same boundary conditions and operating parameters used in the empty pipe simulations were maintained for all rotating configurations equipped with the Kenics mixer. A grid independence study was conducted for the pipe with a Kenics mixer rotating at H/D = 8 and N = 3, and five tetrahedral meshes were generated: 59,137, 123,370, 239,705, 398,957, and 815,211. The percentage difference in the Nusselt number and friction factor between 398,957 and 815,211 was less than 1%. The grid size of 398,957 elements was selected for the study due to computational cost. Prism layers were grown along both the channel wall and the Kenics surfaces to maintain $y^+ \leq 1$ on all solid surfaces across the Re_a range investigated.

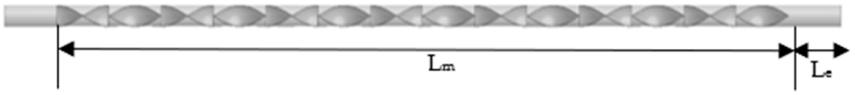


Figure 6. Three-dimensional geometry of the Kenics static mixer with 14 elements used in the simulations.

Table 5. Geometric parameters of pipe insert.

Parameter	Symbol	Value
Mixing zone length	L_m (mm)	700
Insert width	W (mm)	20
Insert thickness	δ (mm)	1
Entrance length	L_e (mm)	50
Twist angle	(°)	180

3. Results and Discussion

3.1. Fluid Flow Under Rotational Motion

The internal flow behavior of the pipe was analyzed using the predicted streamline distributions and velocity contours, as shown in Figure 7. The comparison covered the axial and parallel configurations at N = 1 and Re_a = 5000 for H/D = 2, 4, and 8. Secondary vortices formed distinctly within the pipe cross-section under various rotational conditions. These vortices enhanced radial transport between the near-wall region and the pipe core. This fundamentally altered the momentum distribution compared to the stationary case. The intensified cross-sectional mixing was the primary mechanism behind the Nusselt number elevations reported in Figure 8 (at an aspect ratio, L/D, of 20). As the rotational motion increased, continuous recirculating flow structures formed, further intensifying mixing in the cross-section of the pipe. Notably, the parallel configuration at H/D = 8 generated the most vigorous vortical structures among all the cases examined, consistent with its superior heat transfer performance compared to both the axial configuration and the lower eccentricity ratios.

The behavior arises from the interaction of two orthogonal body forces. Centrifugal acceleration acts radially outward from the rotation axis, while gravity acts vertically downward. In the parallel configuration, these body forces act asymmetrically across the pipe cross-section, distorting the secondary vortices and redistributing momentum in a manner absent from axial rotation. At low eccentricity (H/D = 2), the pipe lies close to the rotation axis. The centrifugal force is therefore weak and the flow asymmetrically moderate.

This explains the comparatively small Nusselt number gain of 46% over axial rotation. As H/D increases, the centrifugal acceleration grows linearly with the radial distance. This progressively intensifies the near-wall vortices and drives the monotonic improvement in thermal performance from H/D = 2 to H/D = 8.

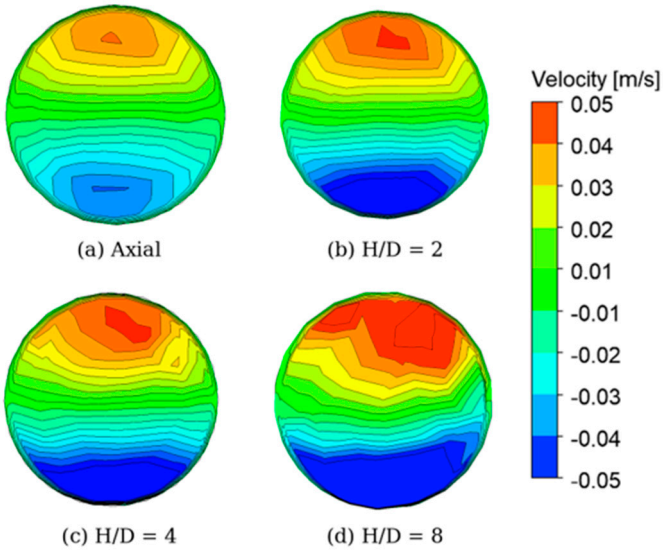


Figure 7. Velocity contours at L/D = 20, N = 1, and Re_a = 5000 for (**a**) axial rotation and parallel rotations at (**b**) H/D = 2, (**c**) H/D = 4, and (**d**) H/D = 8.

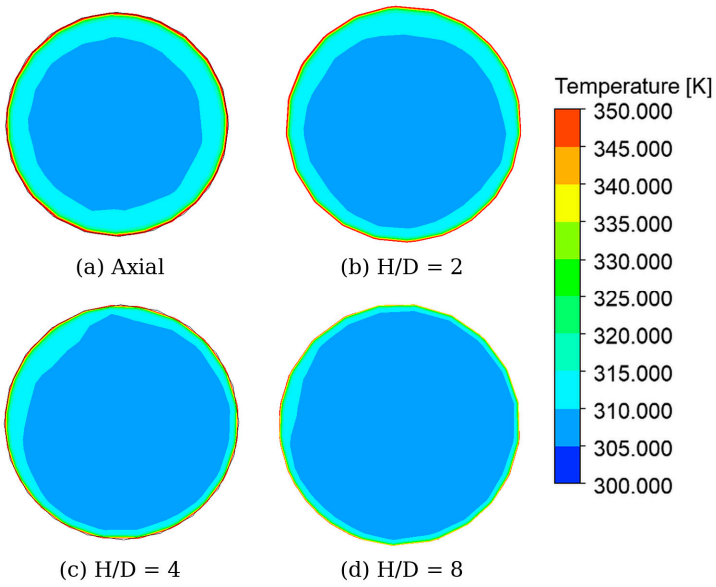


Figure 8. Temperature contours at L/D = 20, N = 1, and Re_a = 5000 for (**a**) axial rotation and parallel rotations at (**b**) H/D = 2, (**c**) H/D = 4, and (**d**) H/D = 8.

As shown in Figure 6, axial rotation produced symmetric Coriolis-driven secondary flows, while the parallel configuration generated stronger cross-sectional distortion through the combined action of centrifugal and Coriolis forces. Note the progressive intensification and growing asymmetry of the high-velocity region from (b) to (d): this visual trend anticipates the Nusselt number ranking quantified in Section 3.3. This asymmetry is the key reason why the parallel configuration consistently outperformed axial rotation in heat transfer across all eccentricity ratios tested.

3.2. Thermal Fluid Distribution and Temperature Behavior

The temperature contours for Re_a = 5000 and N = 1 are shown in Figure 8. The secondary vortices swept high-temperature fluid away from the heated wall and replaced it with cooler core fluid. This thinned the thermal boundary layer and directly increased the Nusselt number (Figure 8). The H/D = 8 case produced the most uniform cross-sectional temperature distribution, consistent with it exhibiting the most vigorous vortical structures. By contrast, the axial rotation case showed the least uniform distribution, reflecting its weaker, purely Coriolis-driven mixing.

The progressive flattening of the thermal gradient from axial rotation through H/D = 2, 4, and 8 confirms that increasing eccentricity enhances cross-sectional thermal mixing, directly correlating with the Nusselt number improvements quantified in Figure 8.

3.3. Thermal Transport Enhancement and Friction Factor

The variations in the Nusselt number for the axial Reynolds numbers and rotation rates investigated (N = 1, 2, 3) are presented in Figure 9. The Nusselt number increased with increasing axial Reynolds number in all cases due to heightened turbulence intensity at higher flow rates, a trend consistent with classical internal flow correlations. Among all configurations, parallel rotation at H/D = 8 delivered the greatest enhancement. At Re_a = 5000 and N = 3, the Nusselt number improved by 88% compared to the axial rotating case. This pronounced advantage over axial rotation stems directly from the stronger centrifugal force at the largest radial offset. The stronger forcing generates more intense secondary vortices and drives mixing deeper into the thermal boundary layer, as visualized in Figures 7 and 8. Enhancement decreased systematically with decreasing eccentricity: 66% for H/D = 4 and 46% for H/D = 2 compared to axial rotation at Re_a = 5000 and N = 3. This confirms that centrifugal acceleration, which scales linearly with radial distance, is the dominant driver of thermal performance in the parallel configuration.

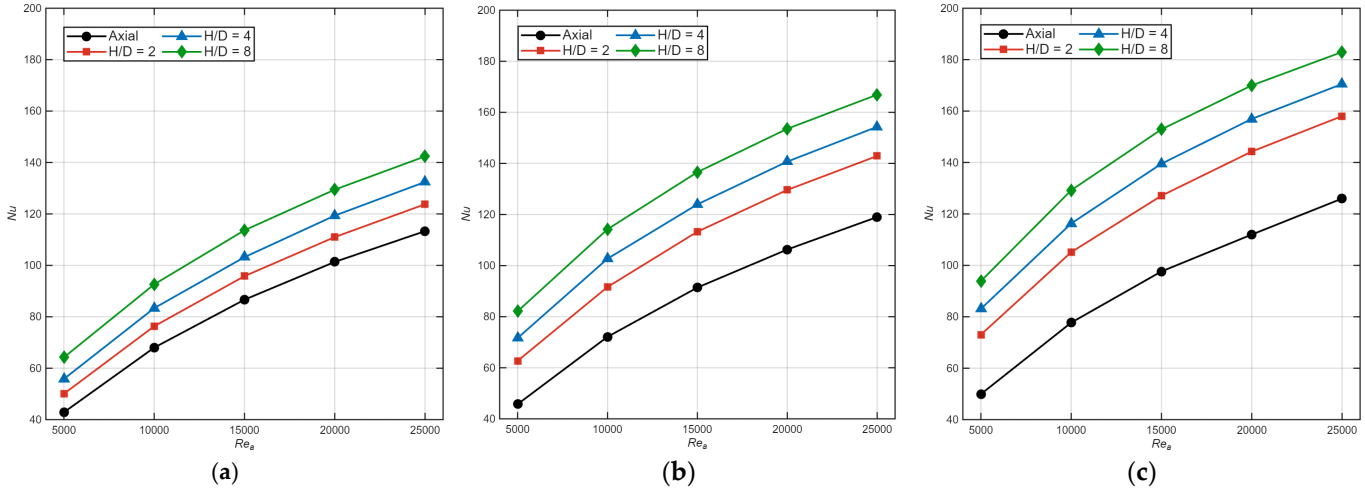


Figure 9. Variation in Nu with Re_a for the axial and parallel rotation configurations at (**a**) N = 1, (**b**) N = 2, and (**c**) N = 3.

Although rotational motion improves thermal transport, it incurs a substantial pressure drop. Figure 10 shows the variation in the friction factor for different axial Reynolds numbers and rotation rates. Parallel rotation at H/D = 8 produced the highest friction factor at Rea = 25,000 and N = 3, approximately 272% above the axial case. This is a direct consequence of the amplified centrifugal forces and stronger near-wall shear at the largest eccentricity. This stands in stark contrast to the axial configuration, where the absence of an offset centrifugal body force limits the hydraulic penalty. The friction

factor decreased monotonically with decreasing eccentricity ratio: in comparison to the axial case, H/D = 4 recorded increases of approximately 214%, while H/D = 2 showed the lowest increases of approximately 131%. This eccentricity-dependent friction trend precisely mirrors the Nusselt number trend documented above. The same centrifugal mechanism that drives heat transfer enhancement therefore amplifies the hydraulic penalty. At higher axial Reynolds numbers, increased turbulence intensity further augmented the pressure drop, and progressively larger penalties were observed as the rotational number increased.

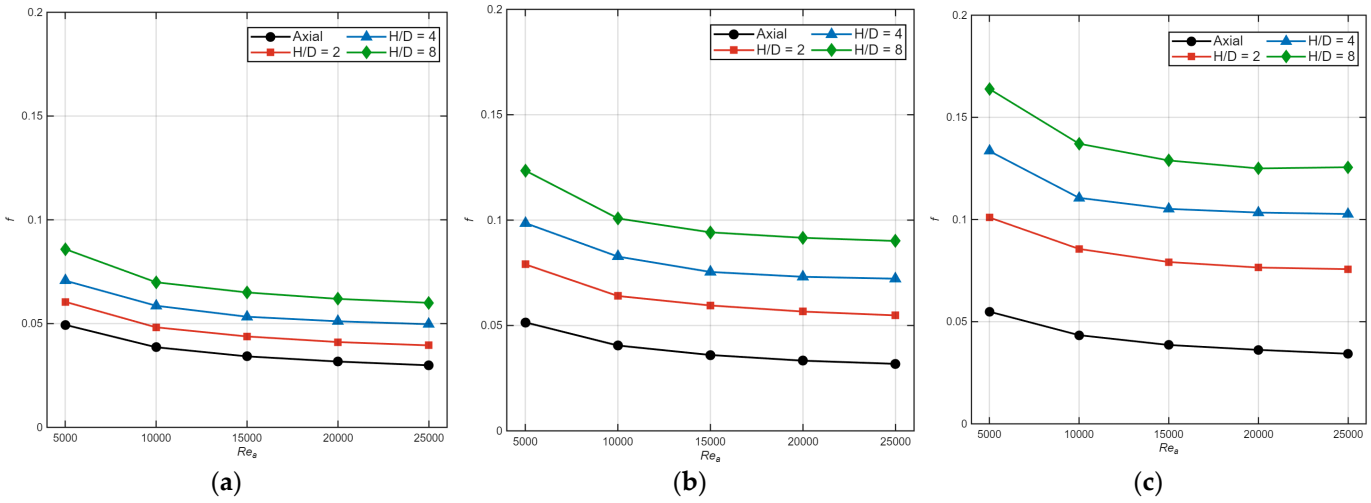


Figure 10. Variation in the friction factor (f) with Re_a for axial and parallel rotational configurations at (**a**) N = 1, (**b**) N = 2, and (**c**) N = 3.

3.4. Kenics Mixer

The introduction of the Kenics mixer significantly altered the internal flow structure of the rotating channel. As shown in Figure 11, the insert produced repeated flow splitting and strong secondary recirculating motion throughout the cross-section. The rotationally induced vortices interacted with the mixer-generated swirl, thereby intensifying radial transport and momentum redistribution beyond what either mechanism achieves independently. This synergy explains why the Kenics mixer configurations consistently outperformed the empty rotating pipe in Nusselt number under equivalent operating conditions. Compared to the empty rotating pipe, the Kenics mixer configuration produced stronger flow skewness and more pronounced cross-sectional flow recirculation. This effect was particularly pronounced in the parallel configuration (H/D = 8), where the already-intense centrifugal vortices were further energized by the mixer, making this the highest-performing configuration in terms of heat transfer.

Note in Figure 10 the pronounced flow splitting on either side of the mixer blade and the stronger velocity skewness in the parallel case (b) than in the axial case (a). Both features indicate more vigorous cross-sectional transport, and they explain why the combined mixer–rotation configuration outperformed either mechanism alone.

Continuous flow reorientation by the mixer disrupted the near-wall thermal layer and enhanced core-to-wall mixing, as illustrated in Figure 12. The mixer reduced convective thermal resistance and produced more uniform temperature distributions than the empty rotating pipe. The parallel H/D = 8 configuration again showed the greatest improvement, consistent with the flow field observations in Figure 11.

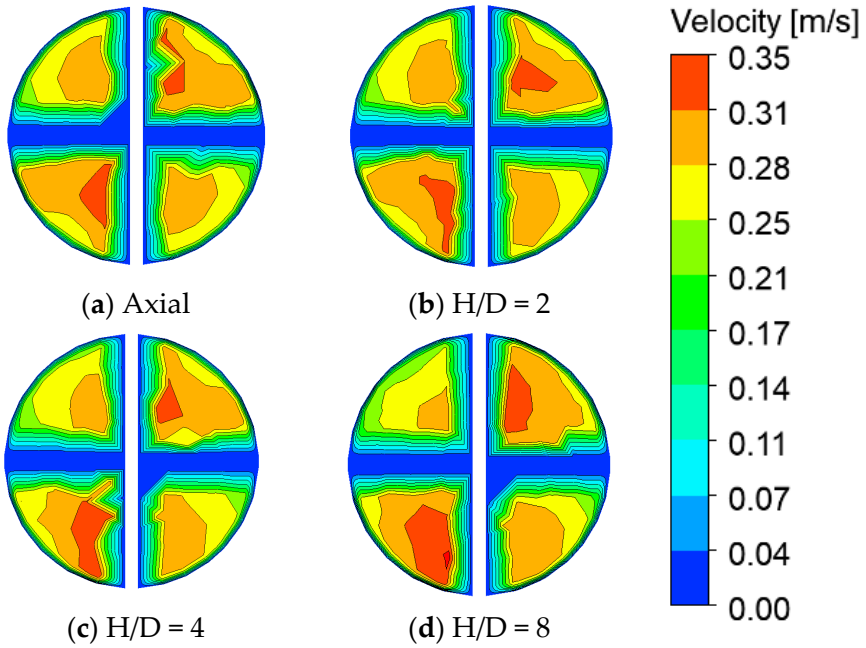


Figure 11. Velocity contours at L/D = 20, N = 1, and Re_a = 5000 showing the influence of the Kenics mixer on vortex development in (**a**) the axial configuration and parallel configurations at (**b**) H/D = 2, (**c**) H/D = 4, and (**d**) H/D = 8.

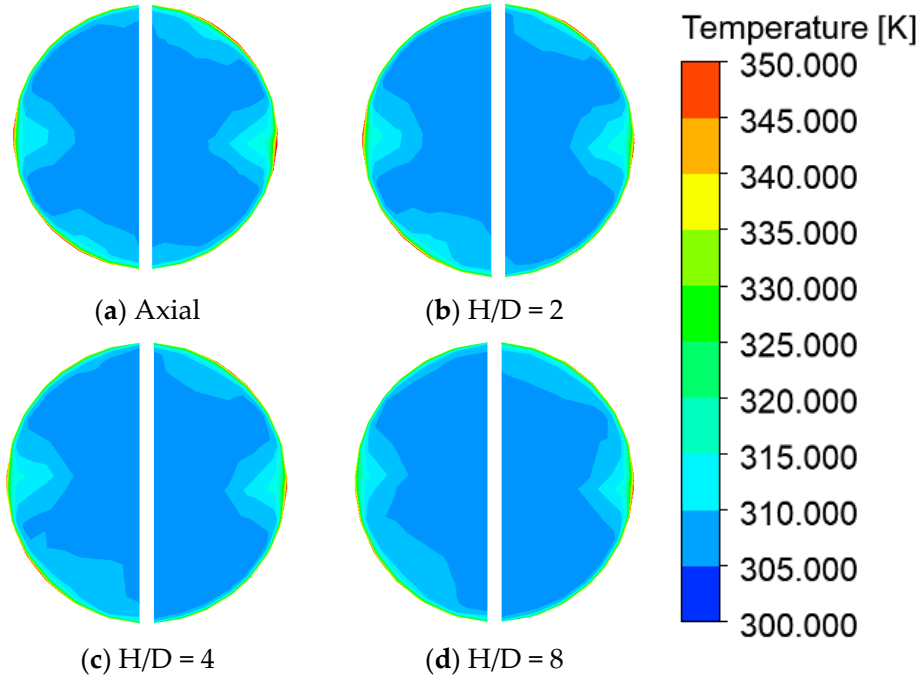


Figure 12. Temperature contours at L/D = 20, N = 1, and Re_a = 5000 showing the influence of the Kenics mixer on thermal mixing in (**a**) the axial configuration and parallel configurations at (**b**) H/D = 2, (**c**) H/D = 4, and (**d**) H/D = 8.

The more uniform temperature field in the H/D = 8 case than in the axial configuration confirms that the mixer's thermal benefit is amplified where rotational vortices are already strongest and that the two enhancement mechanisms act synergistically rather than redundantly.

The Kenics mixer produced substantial Nusselt number enhancement in the axial rotating configuration. However, its additional contribution was less pronounced in parallel rotating channels, particularly at higher rotation numbers. As shown in Figure 13c, some Kenics-equipped configurations exhibited negligible or slightly lower Nusselt numbers compared with their corresponding empty rotating channels. Therefore, the heat-transfer enhancement associated with the Kenics mixer was dependent on the rotational configuration and operating conditions.

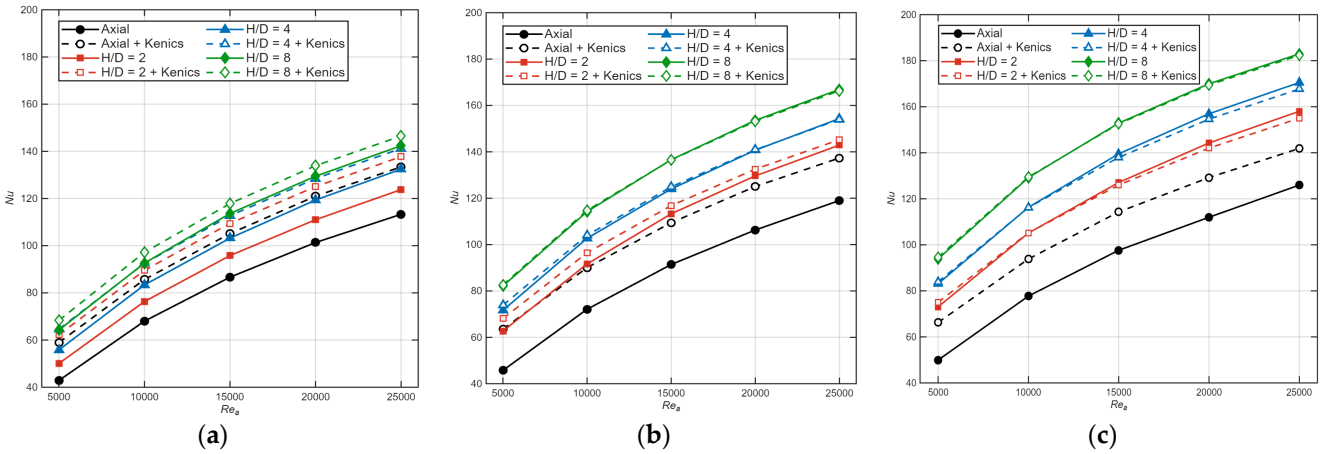


Figure 13. Variation in Nu with Re_a for the rotating channel with and without the Kenics mixer at (**a**) N = 1, (**b**) N = 2, and (**c**) N = 3.

For the axial configuration, the insertion of the Kenics mixer resulted in substantial heat transfer enhancement, with Nusselt number increases of 17–38% at (N = 1), 15–37% at (N = 2), and 13–35% at (N = 3). These results indicate that the insert is most effective when rotational effects alone provide only moderate enhancement. In contrast, the addition of the Kenics mixer to the parallel configuration (H/D = 8) resulted in only marginal improvements. Nusselt number enhancements were limited to 3–8% at (N = 1), decreasing to 0–2% at (N = 2) and 0–1% at (N = 3). These findings have important design implications. At H/D = 8, the Kenics mixer provides limited additional heat-transfer enhancement while introducing a substantial pressure drop penalty, resulting in reduced overall thermo-hydraulic performance. Therefore, the use of Kenics inserts may be more appropriate for axial rotation or low-eccentricity parallel configurations where additional heat-transfer enhancement is prioritized over pumping power requirements.

Despite the significant improvement in heat transfer, the enhanced mixing and stronger recirculating structures resulted in a considerable increase in pressure drop, as indicated in Figure 14. Note the wide gap between the axial with-mixer curve and its empty pipe counterpart, which marks the largest relative penalty observed in this study. Intensified wall shear stresses and momentum losses from repeated obstruction and redirection of flow drove the large increase in friction factors compared to the empty rotating pipe. The axial rotating case recorded the highest friction factor increase of about 700–800% for N = 3. Similarly, the parallel (H/D = 8) configuration showed friction factor increases of approximately 280–310% with the inclusion of the insert. The friction penalty became more profound as the rotational number increased due to the combined influence of rotation-induced vortices and mixer-generated recirculation.

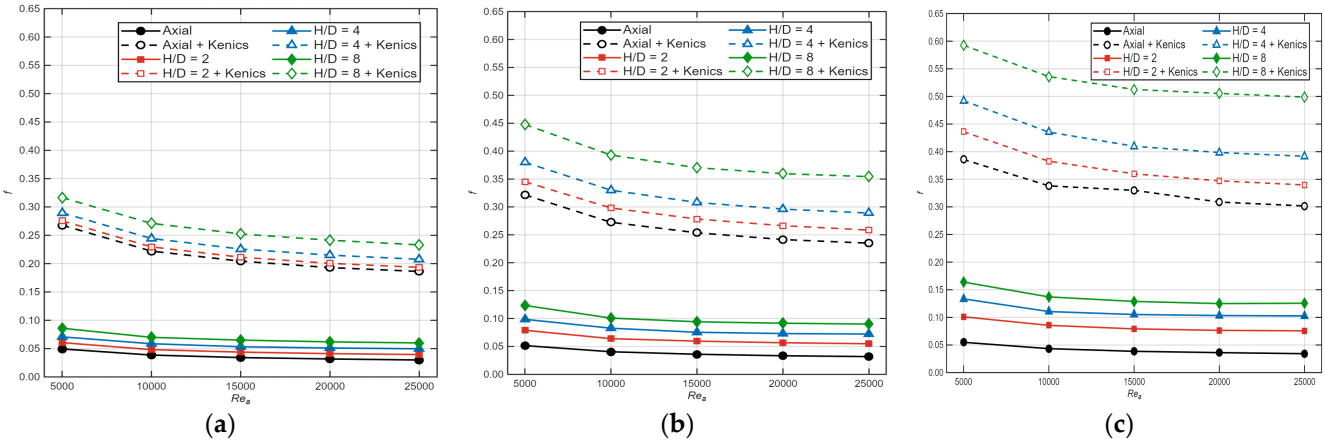


Figure 14. Variation in the friction factor with Re_a for the rotating pipe with and without the Kenics mixer at (**a**) N = 1, (**b**) N = 2, and (**c**) N = 3.

3.5. Thermo-Hydraulic Performance

Sections 3.3 and 3.4 reported the Nusselt number and friction factor separately. These two quantities must be weighed together to assess the net performance: a configuration that enhances Nu but incurs disproportionately large friction penalty does not deliver real benefit on a constant-pumping-power basis. The TPF [42] as shown in Equation (29) captures this trade-off, with values above unity indicating that the heat-transfer outweighs the hydraulic penalty, and values below unity indicating the opposite.

$$\mathrm{TPF} = \frac{\left(\frac{\mathrm{Nu}}{\mathrm{Nu}_0}\right)}{\left(\frac{\mathrm{f}}{\mathrm{f}_0}\right)^{\frac{1}{3}}} \tag{31}$$

where Nu_0 and f_0 are the Nusselt number and friction factor of the stationary smooth pipe, respectively, at the same Re_a.

Two distinct regimes emerged across the dataset. The empty rotation configuration achieved TPF > 1 across the entire parametric study, while every Kenics-equipped case produced TPF < 1. This result deserves careful interpretation. The Kenics mixer delivered substantial heat-transfer enhancement in axial channels, with Nusselt number increases of 17–38% at N = 1, 15–37% at N = 2, and 13–35% at N = 3 (Section 3.4). The accompanying friction factor penalty, however, was large—approximately 700–800% for the axial case at N = 3—and this hydraulic cost consistently exceeded the thermal benefit. The Kenics mixer is therefore an effective heat-transfer enhancer but not an effective thermo-hydraulic enhancer under the rotating conditions investigated.

Among the empty pipe rotating cases, parallel rotation outperformed axial rotation at every Re_a and the margin widened with eccentricity. Under the headline conditions of Re_a = 5000 and N = 3, the parallel H/D = 8 configuration achieved the highest TPF in the study (1.47), a 30% improvement over axial rotation (TPF = 1.13), as shown in Figure 15; the lowest TPF (0.59) was found for axial + Kenics at Re_a = 25,000 and N = 3.

The parallel configurations maintained their TPF advantage over axial rotation from Re_a = 5000 to 20,000. Table 6 extends the comparison to all three rotation rates at Re_a = 5000, where the maximum TPF in the study was observed.

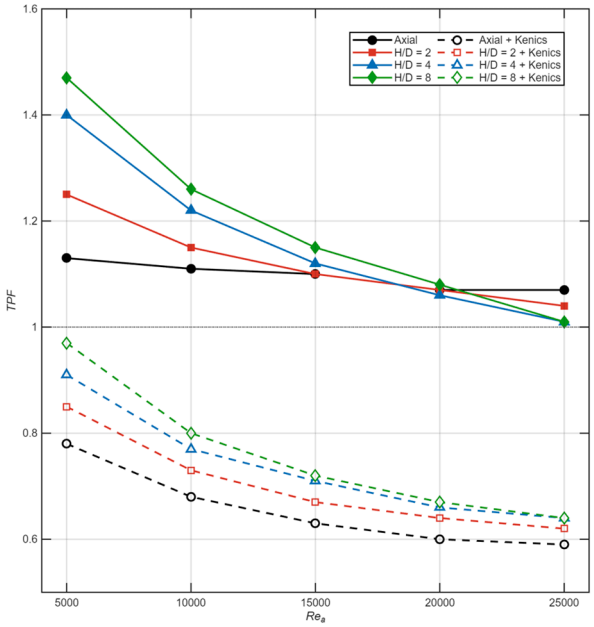


Figure 15. Effect of rotation on thermo-hydraulic performance factor (TPF) at N = 3 for all empty and Kenics mixer configurations.

Table 6. Thermo-hydraulic performance factor (TPF) for all configurations at Re_a = 5000 and N = 1–3.

Configuration	TPF					
	N = 1	N = 1 (Kenics)	N = 2	N = 2 (Kenics)	N = 3	N = 3 (Kenics)
Axial	1	0.78	1.05	0.80	1.13	0.78
H/D = 2	1.09	0.82	1.25	0.83	1.35	0.85
H/D = 4	1.16	0.84	1.33	0.88	1.40	0.91
H/D = 8	1.25	0.86	1.42	0.93	1.47	0.97

The findings reveal a clear distinction between two performance metrics. Based on heat-transfer enhancement alone, the Kenics mixer is most effective in axial and low-eccentricity parallel configurations, where rotational effects alone are insufficient to generate strong secondary flow. When the overall thermo-hydraulic trade-off is considered, however, the mixer does not justify its pressure penalty under any rotating condition tested—rotation alone achieves a favorable TPF > 1 in every configuration. The Kenics insert should therefore be considered where maximum heat-transfer enhancement is prioritized over pumping cost, while parallel rotation at high eccentricity (H/D = 8) remains the preferred strategy when overall net performance is the design objective.

4. Conclusions

A three-dimensional numerical study of turbulent heat transfer and fluid flow was conducted for both axial and parallel rotating heated pipes, covering axial Reynolds numbers of 5000–25,000 and rotation rates of N = 1, 2, and 3. The central finding was that heat-transfer enhancement and overall thermo-hydraulic performance behave as distinct design criteria: every mechanism that enhanced heat transfer—eccentric rotation, higher rotation rate, and the Kenics mixer—also increased the friction penalty, and the two must be weighed together when selecting a configuration. The main conclusions drawn from this investigation are as follows:

1. Both axial and parallel rotational configurations generated well-defined secondary vortical structures that intensified cross-sectional mixing, reduced the thermal boundary layer thickness, and improved convective heat transfer compared to the stationary reference pipe. Under axial rotation, symmetric Coriolis-driven secondary flows developed along the pipe axis, whereas the parallel configuration produced stronger cross-sectional distortion through the combined action of centrifugal and Coriolis body forces acting orthogonally to the pipe axis.
2. Among all empty pipe cases, the parallel configuration at the highest eccentricity ratio (H/D = 8) yielded the greatest thermal enhancement. At Re_a = 5000 and N = 3, the Nusselt number improved by 88% compared to the axial rotating case, owing to the amplified centrifugal body forces at the largest radial offset from the axis of rotation. Eccentricity ratios of H/D = 4 and H/D = 2 yielded improvements of 66% and 46%, respectively, over the axial configuration under the same operating conditions, confirming that centrifugal acceleration scales with radial distance and is the dominant mechanism describing thermal performance in parallel rotation.
3. Thermal enhancement was accompanied by a substantial increase in the pressure drop penalty. The parallel configuration at H/D = 8, Re_a = 25,000, and N = 3 incurred the highest friction factor increase, approximately 272% above that of the axial rotating case.
4. The introduction of the Kenics static mixer into the rotating pipe significantly intensified the secondary recirculating flow through repeated flow splitting and reorientation, producing more uniform cross-sectional temperature distributions and a thinner convective thermal boundary layer than the empty rotating pipe under equivalent operating conditions. The synergistic interaction between rotationally induced vortices and mixer-generated swirl was particularly pronounced in the parallel configuration at H/D = 8, where the combined enhancement exceeded that of either mechanism acting independently.
5. The Kenics mixer provided additional heat-transfer enhancement, with Nusselt number increases of 17–38% in axial channels but only 0–8% at H/D = 8, where rotation already saturates the available enhancement. This gain was accompanied by substantial friction factor increases, reaching 700–800% for the axial case at N = 3. The Kenics mixer is therefore most effective, in terms of heat-transfer enhancement, in axial and low-eccentricity configurations where rotation alone provides only moderate enhancement, with lower rotation numbers (N = 1) offering the most favorable Nu-to-friction trade-off.
6. Thermal Performance Factor (TPF) analysis against the stationary smooth pipe benchmark revealed that all empty pipe rotating configurations achieved TPF > 1, with the maximum TPF occurring for the parallel H/D = 8 configuration at Re_a = 5000 and N = 3. In contrast, all configurations with the Kenics mixer produced TPF < 1 across the full parameter space tested. Rotation alone therefore provides thermo-hydraulically favorable enhancement, while Kenics insertion imposes a pressure penalty that exceeds its thermal benefit under rotation regardless of eccentricity or operating conditions. The parallel configuration at high eccentricity emerged as the thermo-hydraulically optimal design for rotating cooling channels in high-power-density electric machines. The choice between insert-based augmentation and bare rotation therefore depends on which performance criterion—heat transfer alone or overall thermo-hydraulic efficiency—is prioritized for the application.

Author Contributions: Conceptualization, K.Y.A. and O.Y.W.A.; methodology, K.Y.A.; software, J.P.K.; validation, A.A.-M.; formal analysis, Y.T.; investigation, K.Y.A.; resources, J.P.K.; data curation, K.Y.A.; writing—original draft preparation, K.Y.A.; writing—review and editing, O.Y.W.A. and

R.O.; visualization, K.Y.A.; supervision, O.Y.W.A. and J.P.K.; project administration, J.P.K.; funding acquisition, J.P.K. All authors have read and agreed to the published version of the manuscript.

Funding: The authors acknowledge the support from NASA NNH16ZEA001N: Electric Propulsion: Challenges and Opportunities.

Data Availability Statement: All data files are available upon request.

Conflicts of Interest: The authors declare no conflicts of interest.

Abbreviations

The following abbreviations are used in this manuscript:

Symbol	Definition	Unit
A_s	Wall surface area	m^2
C_p	Specific heat at constant pressure	J/kg-K
C_μ	Coefficient in the turbulence model	
D	Pipe diameter	m
g	Gravitational acceleration	m/s^2
h	Convective heat transfer coefficient	W/m^2-K
H	Eccentricity length	m
k	Thermal conductivity	W/m-K
L	Pipe length	m
L_e	Entrance length	m
L_m	Mixing zone length	m
P	Pressure	Pa
q_w	Heat flux	W/m^2
T	Temperature	K
T_s	Wall (surface) temperature	K
T_b	Bulk temperature	K
U	Bulk (inlet) velocity	m/s
V_r	Radial velocity	m/s
V_z	Axial velocity	m/s
V_θ	Azimuthal velocity	m/s
W	Insert width	m
Greek symbols		
β	Coefficient of thermal expansion	K^{-1}
δ	Insert thickness	m
μ	Dynamic viscosity	kg/m-s
ν	Kinematic viscosity	m^2/s
ρ	Density	kg/m^3
Ω	Angular velocity	s^{-1}
Non-dimensional group		
f	Friction factor	
Gr_g	Gravitational Grashof number	
Gr_Ω	Rotational Grashof number	
N	Rotation rate	
Nu	Nusselt number	
Nu_s	Nusselt number of stationary channel	
Pr	Prandtl number	
Re_a	Axial Reynolds number	
Re_Ω	Rotational Reynolds number	
H/D	Eccentricity ratio	
L/D	Aspect ratio	

References

1. Boglietti, A.; Cavagnino, A.; Staton, D.; Shanel, M.; Mueller, M.; Mejuto, C. Evolution and Modern Approaches for Thermal Analysis of Electrical Machines. *IEEE Trans. Ind. Electron.* **2009**, *56*, 871–882. [CrossRef]
2. Tighe, C.; Gerada, C.; Pickering, S. Assessment of cooling methods for increased power density in electrical machines. In *Proceedings of the 2016 XXII International Conference on Electrical Machines (ICEM), Lausanne, Switzerland, 4–7 September 2016*; IEEE: Piscataway, NJ, USA, 2016; pp. 2626–2632. [CrossRef]

3. McCluskey, P.; Saadon, Y.; Yao, Z.; Shah, J.; Kizito, J. Thermal management challenges in turbo-electric and hybrid electric propulsion. In Proceedings of the 2018 International Energy Conversion Engineering Conference, Cincinnati, OH, USA, 9–12 July 2018.
4. Pedley, T.J. On the instability of rapidly rotating shear flows to non-axisymmetric disturbances. *J. Fluid Mech.* **1968**, *31*, 603–607. [CrossRef]
5. Borisenko, A.I.; Kostikov, O.N.; Chumachenko, V.I. Experimental study of turbulent flow in a rotating channel. *J. Eng. Phys.* **1973**, *24*, 770–773. [CrossRef]
6. White, A. Flow of a fluid in an axially rotating pipe. *J. Mech. Eng. Sci.* **1964**, *6*, 47–52. [CrossRef]
7. Seghir-Ouali, S.; Saury, D.; Harmand, S.; Phillipart, O.; Laloy, D. Convective heat transfer inside a rotating cylinder with an axial air flow. *Int. J. Therm. Sci.* **2006**, *45*, 1166–1178. [CrossRef]
8. Abotsi, O.Y.W. Development of Cooling Techniques for Electric Machines at High Rotational Rayleigh Number. Doctoral Dissertation, North Carolina Agricultural and Technical State University, Greensboro, NC, USA, 2021.
9. Humphreys, J.; Morris, W.; Barrow, H. Convection heat transfer in the entry region of a tube which revolves about an axis parallel to itself. *Int. J. Heat Mass Transfer* **1967**, *10*, 333–340. [CrossRef]
10. Morris, W.D.; Dias, F.M. Turbulent heat transfer in a revolving square-sectioned tube. *J. Mech. Eng. Sci.* **1980**, *22*, 95–101. [CrossRef]
11. Fasquelle, A.; Pellé, J.; Harmand, S.; Shevchuk, I.V. Numerical study of convective heat transfer enhancement in a pipe rotating around a parallel axis. *J. Heat Transf.* **2014**, *136*, 051901. [CrossRef]
12. Wang, J.; Jahns, T.M.; McCluskey, P.; Kizito, J.; Sarlioglu, B.; Borjas, R.; Swanke, J.A.; Cong, Y.; Yao, Z.; Zeng, H.; et al. 2-kV 1-MW 20000-r/min Integrated Modular Motor Drive for Electrified Aircraft Propulsion. *IEEE J. Emerg. Sel. Top. Power Electron.* **2023**, *13*, 394–407. [CrossRef]
13. Varun; Garg, M.; Nautiyal, H.; Khurana, S.; Shukla, M. Heat transfer augmentation using twisted tape inserts: A review. *Renew. Sustain. Energy Rev.* **2016**, *63*, 193–225. [CrossRef]
14. Kumar, L.; Yadav, V.K.; Singh, S.K.; Kacker, R.; Srivastava, H.V. Effect of twisted tape with rotating vane angles on performance of double-pipe heat exchanger. *Proc. Inst. Mech. Eng. Part E J. Process Mech. Eng.* **2025**, *240*, 5368–5382. [CrossRef]
15. Arasteh, H.; Rahbari, A.; Mashayekhi, R.; Keshmiri, A.; Mahani, R.B.; Talebizadehsardari, P. Effect of pitch distance of rotational twisted tape on the heat transfer and fluid flow characteristics. *Int. J. Therm. Sci.* **2021**, *170*, 106966. [CrossRef]
16. Song, Y.-Q.; Izadpanahi, N.; Fazilati, M.A.; Lv, Y.-P.; Toghraie, D. Numerical analysis of flow and heat transfer in an elliptical duct fitted with two rotating twisted tapes. *Int. Commun. Heat Mass Transf.* **2021**, *125*, 105328. [CrossRef]
17. Nakhchi, M.; Hatami, M.; Rahmati, M. Experimental evaluation of performance intensification of double-pipe heat exchangers with rotary elliptical inserts. *Chem. Eng. Process.-Process Intensif.* **2021**, *169*, 108615. [CrossRef]
18. Dabestani, A.; Kahani, M. CFD analysis of rotation effect on flow patterns and heat transfer enhancement in a horizontal spiral tube heat exchanger. *Case Stud. Therm. Eng.* **2024**, *64*, 105494. [CrossRef]
19. Fang, Z.; Zhao, C.; Li, H. Thermal performance enhancement and multi-parameter optimization of an innovative double helical fin-reinforced coaxial casing geothermal heat exchanger. *Appl. Therm. Eng.* **2025**, *280*, 128145. [CrossRef]
20. Abou-Ziyan, H.; Ameen, R.; Elsayed, K. Fluid flow and convection heat transfer in concentric and eccentric cylindrical annuli of different radii ratios for Taylor-Couette-Poiseuille flow. *Adv. Mech. Eng.* **2021**, *13*, 16878140211040731. [CrossRef]
21. Sun, S.-L.; Liu, D.; Dong, D.-W.; Song, Y.-Z.; Ye, D.; Kim, H.-B. Effects of axial elliptical slit on convective heat transfer and entropy generation evaluation in Taylor–Couette flow. *Int. Commun. Heat Mass Transf.* **2025**, *163*, 108722. [CrossRef]
22. Bahrami, H.R.T.; Safikhani, H. Heat transfer enhancement inside an eccentric cylinder with an inner rotating wall using porous media: A numerical study. *J. Therm. Anal. Calorim.* **2020**, *141*, 1905–1917. [CrossRef]
23. Zhang, S.; Lu, L.; Dong, C.; Cha, S.H. Performance evaluation of a double-pipe heat exchanger fitted with self-rotating twisted tapes. *Appl. Therm. Eng.* **2019**, *158*, 113770. [CrossRef]
24. Liang, C.; Rao, Y. Numerical study of turbulent flow and heat transfer in channels with detached pin fin arrays under stationary and rotating conditions. *Int. J. Therm. Sci.* **2021**, *160*, 106659. [CrossRef]
25. Jing, Q.; Xie, Y.; Zhang, D. Numerical investigation of flow and heat transfer in rotating trapezoidal channel with lateral slots and dimple structure. *Int. Commun. Heat Mass Transf.* **2020**, *118*, 104865. [CrossRef]
26. Shi, D.; Jing, Q.; Gao, T.; Zhang, D.; Xie, Y. Flow and heat transfer mechanism of U-shaped channel considering variable cross-section and rotating effects. *Int. Commun. Heat Mass Transf.* **2021**, *129*, 105701. [CrossRef]
27. Cao, Z.; Luo, L.; Yang, X.; Yan, H.; Du, W. Effects of turning vane on flow control and heat transfer in ribbed two-pass channel with varied rib patterns. *Int. J. Therm. Sci.* **2025**, *207*, 109342. [CrossRef]
28. Choi, S.; Park, H.S.; Heo, J.; Kim, J.; Cho, H.H. Detailed heat and mass transfer of rotor-stator systems with radial rib structures on the rotating disk. *Int. Commun. Heat Mass Transf.* **2025**, *162*, 108670. [CrossRef]
29. Yan, H.; Luo, L.; Zhang, J.; Du, W.; Wang, S.; Huang, D. Flow structure and heat transfer characteristics of a pin-finned channel with upright/curved/inclined pin fins under stationary and rotating conditions. *Int. Commun. Heat Mass Transf.* **2021**, *127*, 105483. [CrossRef]

30. Chia, K.; Huang, S.; Liu, Y. Experimental investigation of heat transfer on the internal tip wall in a rotating two-pass rectangular channel. *J. Therm. Sci. Eng. Appl.* **2021**, *13*, 011025. [CrossRef]
31. Zhang, B.; Zhu, H.; Liu, C. Effects of rotation number on heat transfer and fluid flow in a three-pass serpentine passage with lateral outflow. *J. Therm. Anal. Calorim.* **2021**, *143*, 309–325. [CrossRef]
32. Abotsi, O.Y.; Kizito, J.P. Turbulent heat transfer enhancement in an axially rotating pipe fitted with Kenics segment mixer. *Results Eng.* **2020**, *7*, 100146. [CrossRef]
33. Abotsi, O.Y.W.; Kizito, J.P. Numerical study of heat transfer augmentation in an axially rotating pipe equipped with Kenics mixer. *Case Stud. Therm. Eng.* **2020**, *21*, 100695. [CrossRef]
34. Wang, L.; Wang, S.; Wen, F.; Zhou, X.; Wang, Z. Heat transfer and flow characteristics of U-shaped cooling channels with novel wavy ribs under stationary and rotating conditions. *Int. J. Heat Mass Transf.* **2018**, *126*, 312–333. [CrossRef]
35. Xie, G.; Lei, J.; Deng, X.; Wang, J.; Chen, H. Numerical investigation on two-phase oscillating flow and heat transfer enhancement for a cooling channel with ribs. *Int. J. Therm. Sci.* **2023**, *187*, 108191. [CrossRef]
36. Leung, W.W.; Ren, Y. Scale-up on mixing in rotating microchannel under subcritical and supercritical operating modes. *Int. J. Heat Mass Transf.* **2014**, *77*, 157–172. [CrossRef]
37. Roy, P.; Anand, N.K.; Banerjee, D. A review of flow and heat transfer in rotating microchannels. *Procedia Eng.* **2013**, *56*, 7–17. [CrossRef]
38. ANSYS, Inc. *ANSYS Fluent Theory Guide (Release 2024 R2)*; ANSYS, Inc.: Canonsburg, PA, USA, 2024.
39. Luo, X.; Zhao, X.; Wang, L.; Wu, H.; Xu, G. Flow structure and heat transfer characteristics in rotor–stator cavity with inlet at low radius. *Appl. Therm. Eng.* **2014**, *70*, 291–306. [CrossRef]
40. Nguyen, T.D.; Harmand, S. Heat transfer and vortical structures around a rotating cylinder with a spanwise disk and low-velocity crossflow. *Int. J. Heat Mass Transf.* **2013**, *64*, 1014–1030. [CrossRef]
41. Baudoin, B. Contribution a L'etude des Conditions D'ecoulement Dans le Circuit de Refroidissement D'un Moteur Electrique de Type Ouvert. Doctoral Dissertation, Université de Poitiers, Poitiers, France, 1987. (In French)
42. Webb, R.L. Performance evaluation criteria for use of enhanced heat transfer surfaces in heat exchanger design. *Int. J. Heat Mass Transf.* **1981**, *24*, 715–726. [CrossRef]

Disclaimer/Publisher's Note: The statements, opinions and data contained in all publications are solely those of the individual author(s) and contributor(s) and not of MDPI and/or the editor(s). MDPI and/or the editor(s) disclaim responsibility for any injury to people or property resulting from any ideas, methods, instructions or products referred to in the content.